A locally activatable sensor for robust quantification of organellar glutathione

Sarah Emmert [1,2], **Gianluca Quargnali** [1], **Sebastian Thallmair** [3] & **Pablo Rivera-Fuentes** [1,2] ✉

Glutathione (GSH) is the main determinant of intracellular redox potential and participates in multiple cellular signalling pathways. Achieving a detailed understanding of intracellular GSH homeostasis depends on the development of tools to map GSH compartmentalization and intra-organelle fluctuations. Here we present a GSH-sensing platform for live-cell imaging, termed targetable ratiometric quantitative GSH (TRaQ-G). This chemogenetic sensor possesses a unique reactivity turn-on mechanism, ensuring that the small molecule is only sensitive to GSH in a desired location. Furthermore, TRaQ-G can be fused to a fluorescent protein to give a ratiometric response. Using TRaQ-G fused to a redox-insensitive fluorescent protein, we demonstrate that the nuclear and cytosolic GSH pools are independently regulated during cell proliferation. This sensor was used in combination with a redox-sensitive fluorescent protein to quantify redox potential and GSH concentration simultaneously in the endoplasmic reticulum. Finally, by exchanging the fluorescent protein, we created a near-infrared, targetable and quantitative GSH sensor.

Glutathione (GSH) is a small peptide (L-γ-glutamyl-L-cysteinyl glycine) that can react as a nucleophile or a reducing agent. Upon oxidation, it forms a disulfide-bonded dimer (GSSG). Owing to its high concentration in the cell ($\sim 10^{-3}$ M)[1], the GSH/GSSG pair acts as the main intracellular redox buffer, plays a key role in the detoxification of reactive oxygen species (ROS), and participates in redox signalling[2]. Furthermore, the concentration of GSH and the GSH/GSSG ratio vary between intracellular organelles, and this compartmentalization is actively regulated in the cell[3]. Consequently, disruption of intracellular GSH homeostasis is linked to many pathologies, including cancer[4], diabetes[5] and neurodegenerative disorders[6]. A detailed understanding of the mechanisms of intracellular redox homeostasis and their connection to disease depends on our ability to quantify, among other parameters, changes in GSH concentration in specific organelles. There is thus a need for robust tools that can quantify this critical redox modulator with subcellular specificity.

The GSH/GSSG ratio can be measured in specific organelles using redox-sensitive green fluorescent proteins (roGFPs), particularly those fused to the GSH-specific Grx1 protein[7]. Despite their usefulness, these proteins operate at short wavelengths (<450 nm), display modest brightness and have limited dynamic ranges[8]. Small-molecule sensors have been a popular choice to measure total GSH concentrations. Most of these probes are π-conjugated electrophiles that change their fluorescence upon reaction with GSH. Notable examples include coumarin[9–12] and silicon rhodamine (SiR)[13] dyes. The latter are particularly useful because of their redshifted excitation, selectivity, reversibility and fast kinetics. Targeting small molecules to specific subcellular compartments, however, is challenging. In the case of GSH sensing, the problem is even more difficult, because, to reach its intended organelle, the small molecule must cross the cytosol, where the concentration of GSH is in the range of 10^{-3} M. Accordingly, sensors could react with GSH in the cytosol, and it is difficult to assess whether small molecules actually sense the real concentrations of GSH in their target organelle or shuttle GSH from the cytosol. In fact, a similar question could be asked of any other targeted small-molecule fluorescent sensor. With this limitation in mind, we set out to develop a GSH sensor that is locally activated in the compartment of interest, thus providing a reliable measure of intra-organelle GSH concentrations.

We based our design on the reactivity of SiR dyes, which in their zwitterionic form can serve as electrophiles that react with GSH (Fig. 1a)[13].

[1]Institute of Chemical Sciences and Engineering, Ecole Polytechnique Fédéral de Lausanne, Lausanne, Switzerland. [2]Department of Chemistry, University of Zurich, Zurich, Switzerland. [3]Frankfurt Institute for Advanced Studies, Frankfurt am Main, Germany. ✉e-mail: pablo.riverafuentes@uzh.ch
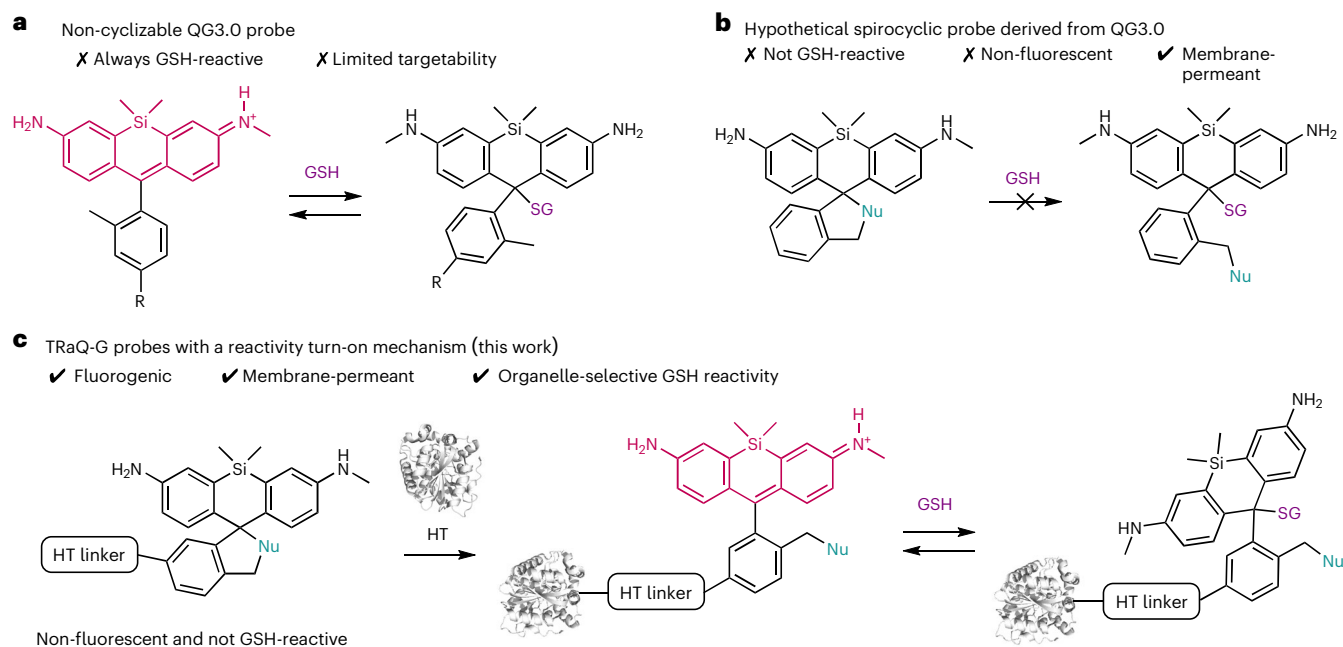
Fig. 1 | Previously reported SiR-based GSH sensors and the TRaQ-G sensing concept. a, Sensing mechanism of the QG3.0 probe[13]. **b**, Hypothetical spirocyclic probe that is both non-fluorescent and non-reactive against GSH. **c**, Sensing concept with the TRaQ-G sensor (this work). R, short linker and secondary small-molecule fluorophore for ratiometric imaging; HT, HaloTag protein; HT linker, chloroalkane substrate.

We hypothesized that a SiR dye in a spirocyclic form would be non-reactive against GSH (Fig. 1b), but it could isomerize to its zwitterionic form upon binding to the self-labelling protein HaloTag (HT)[14–16], switching both its fluorescence and reactivity against GSH from an 'off' to an 'on' state. Moreover, this hybrid sensor design combines the advantages of genetically encoded sensors, such as precise targetability, with the tunability, brightness and photostability of small molecules. Finally, by fusing a fluorescent protein (FP) to HT, we could have an internal standard for ratiometric measurements. We call this design a 'targetable ratiometric quantitative GSH' (TRaQ-G) probe (Fig. 1c).

Results and discussion

Structure–reactivity analysis of TRaQ-G probes

Our first goal was to demonstrate that a known SiR-based GSH sensor, QG3.0[13], retained its reactivity towards GSH when bound to HT. We therefore substituted the reference fluorophore of QG3.0 with a chloroalkane linker, a substrate that reacts with HT (Fig. 2a). The SiR unit was synthesized according to the reported procedure[13], and the linker was attached via amide coupling (Supplementary Scheme 1) to give the Me–TRaQ-G ligand. Using this molecule, we prepared and purified the HT adduct (Methods), Me–TRaQ-G. The reactivity of Me–TRaQ-G against GSH was nearly identical to that of QG3.0 (Fig. 2c and Extended Data Fig. 1a–c)[13], suggesting that one face of the xanthene π-system of Me–TRaQ-G must be exposed to the solvent, thus allowing for GSH nucleophilic attack. This hypothesis was confirmed by X-ray diffraction studies of the adduct, which revealed that the methyl group of the Me–TRaQ-G ligand fits into a shallow hydrophobic pocket created by residues F152, V167 and T172 of HT, exposing the opposite face of the xanthene core to the solvent (Fig. 2a). Furthermore, molecular dynamics (MD) simulations based on the crystal structure indicate that this orientation of the ligand is preferred over the conformation in which the methyl group is exposed to the solvent (Extended Data Fig. 1d,e).

Next, we tested whether SiR derivatives that undergo spirocyclization could become reactive against GSH upon binding to HT. For this purpose, we prepared derivatives in which either a carboxylic acid (Fig. 2b)[14] or a cyanamide (Fig. 2d)[16] nucleophile could form the spirocycle. The syntheses of these probes were adapted from published procedures (Supplementary Schemes 2 and 3)[14,16]. Both ligands were obtained in their spirocyclic form and reacted only very slowly (TRaQ-G) or not at all (TRaQ-G-ctrl) with GSH, as judged by mass spectrometry (Supplementary Fig. 1). Upon reaction with HT, both ligands produced intensely blue solutions, indicating that the zwitterionic form of the SiR core is formed. GSH titration experiments revealed that, whereas the HT-bound carboxylic-acid derivative was completely insensitive to GSH, the cyanamide ligand bound to HT responded to GSH in the physiologically relevant range of concentrations (-1–20 mM; Fig. 2c). We further confirmed that this probe is susceptible only to the absolute GSH concentration, not to the GSH/GSSG ratio (Supplementary Fig. 2a), and that GSH binding is reversible (Supplementary Fig. 2b). Furthermore, no other common intracellular nucleophiles reacted with the probe at physiologically relevant concentrations (Supplementary Fig. 2c). Photophysical characterization of our sensor revealed suitable properties for live-cell imaging in terms of spectral properties, brightness and dynamic range (Supplementary Fig. 3 and Supplementary Tables 1 and 2). We envisioned that the carboxylic-acid derivative, which is insensitive to GSH, could be used as a control probe in quantitative studies. We thus refer to the HT-bound carboxylic-acid derivative as TRaQ-G-ctrl, whereas the cyanamide derivative is hereafter called TRaQ-G.

To understand the difference in reactivity between TRaQ-G-ctrl and TRaQ-G, we analysed the structure of both conjugates by X-ray diffraction. In TRaQ-G-ctrl, the xanthene core of the SiR dye rests on top of the hydrophobic surface created by residues F152, V167 and T172 of HT, and the carboxylate group points outwards into the solvent (Fig. 2b). MD simulations indicate that this conformation is very stable, arguably because of solvation of the carboxylate moiety and additional hydrogen bonding from the secondary amine of the ligand to residue E170 (Supplementary Fig. 4). This carboxylate, and its solvation sphere, efficiently block GSH attack, as observed in GSH titrations (Fig. 2c). In the case of TRaQ-G, we found two distinct monomers in the unit cell, one in which the ligand is in the spirocyclic form (Fig. 2d (bottom left)) and the other in which the xanthene is in the zwitterionic form (Fig. 2d (top right)). Whereas the spirocyclic form binds similarly to
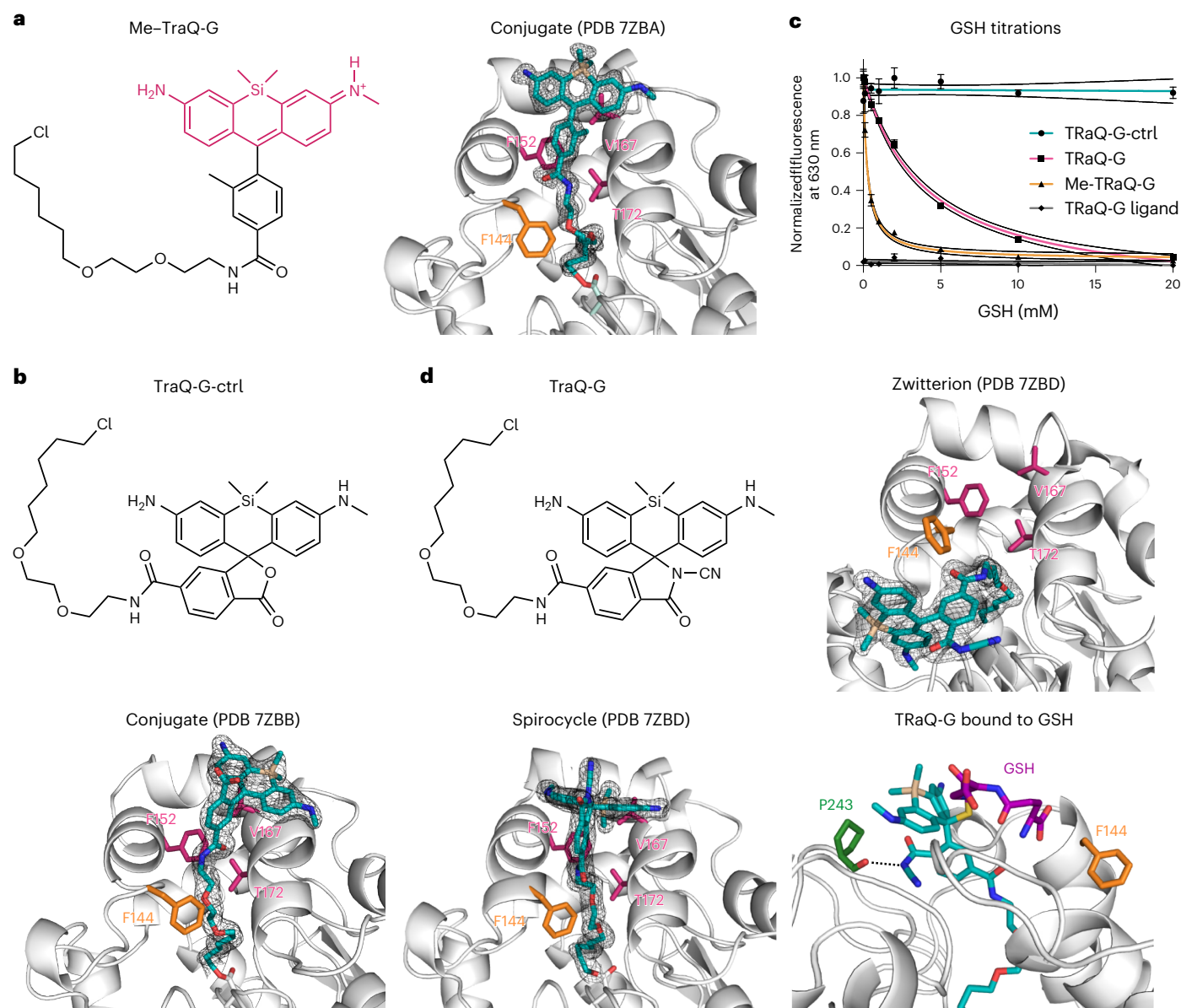
a Me–TraQ-G

Conjugate (PDB 7ZBA)

b TraQ-G-ctrl

c GSH titrations

TRaQ-G-ctrl
TRaQ-G
Me-TRaQ-G
TRaQ-G ligand

d TraQ-G

Zwitterion (PDB 7ZBD)

Conjugate (PDB 7ZBB)

Spirocycle (PDB 7ZBD)

TRaQ-G bound to GSH

Fig. 2 | Structures and reactivity of TRaQ-G probes. a, Chemical structure of the small-molecule ligand for Me–TRaQ-G (left) and the X-ray crystal structure (right) of the ligand–protein conjugate (1.23 Å). **b**, Chemical structure of the small-molecule ligand for TRaQ-G-ctrl (top) and the X-ray crystal structure of the ligand–protein conjugate (1.95 Å) (bottom). **c**, GSH titrations of the three TRaQ-G probes and the TRaQ-G ligand (free small molecule). The concentration of the TRaQ-G probe was kept at 5–15 μM. $N = 3$ independently prepared samples were examined over three independent measurements. Data are presented as mean values, and error bars indicate the standard deviation. **d**, Chemical structure of

the small-molecule ligand for TRaQ-G (top left), and the X-ray crystal structures of TRaQ-G (1.69 Å), displaying the SiR ligand in the spirocyclic (bottom left) and zwitterionic (top right) forms, and a snapshot at 500 ns of the MD simulation of TRaQ-G with GSH bound (bottom right). Residues forming the hydrophobic pocket are displayed in pink, the Phe residue that moves between the open and closed conformations is displayed in orange, and the residue forming a hydrogen bond with the ligand is displayed in green. The 2Fo-Fc electron density map is displayed around the ligand with a standard deviation of all density values (σ) of 1.

Me–TRaQ-G and TRaQ-G-ctrl, the zwitterionic form occupies an alternative pocket. MD simulations using the spirocyclic form as a starting point suggest that the side chain of residue F144 must rotate to allow for the ligand to occupy the alternative pocket and thus switch to its zwitterionic form (Supplementary Fig. 5). Although mutation of this residue does not seem to increase the brightness of SiR-carboxylate dyes[17], this residue could be important to create HT mutants that induce larger fluorogenicity in other SiR-based spirocyclic dyes. Using MD simulations starting from the zwitterionic structure, we found that the structure rapidly relaxes to a stable conformation in which the cyanamide forms a persistent hydrogen bond with the backbone carbonyl of residue P243 (Extended Data Fig. 2). This interaction exposes

the opposite face of the SiR dye to the solvent, allowing for GSH attack (Fig. 2d (bottom right)), explaining the reactivity observed in titration experiments (Fig. 2c).

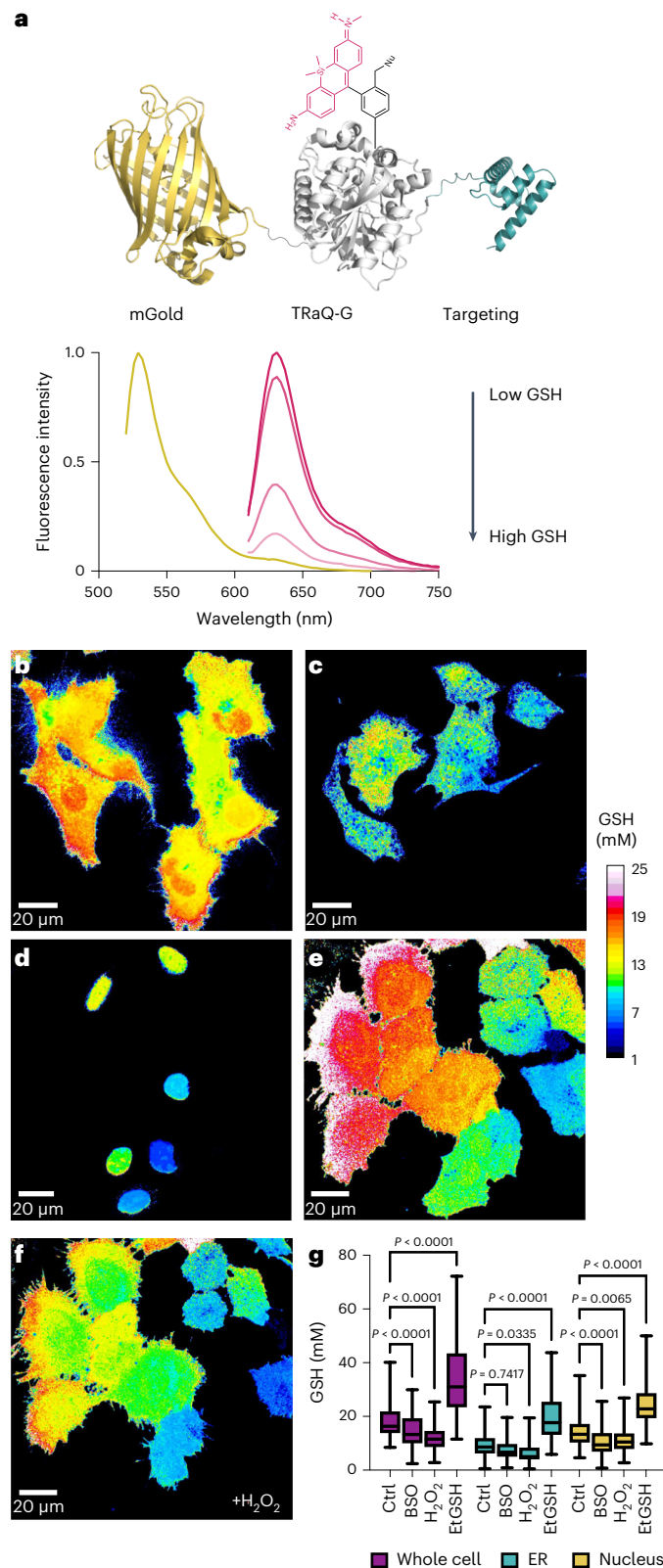**TRaQ-G is a robust, targetable and quantitative GSH sensor**
Although Me–TRaQ-G is sensitive towards GSH, we envisioned that it would perform poorly in live cells given its constant fluorescence and reactivity towards GSH. This suspicion was confirmed by imaging cells expressing HT in the nucleus, which revealed unacceptable levels of off-target signals (Supplementary Fig. 6). Instead, we focused on TRaQ-G, the ligand of which undergoes fluorescence and reactivity turn-on upon binding to HT. Once bound to HT, the strong fluorescence

of the TRaQ-G ligand decreases upon reaction with GSH. This turn-off behaviour can be converted into a ratiometric readout by the presence of an internal standard that is insensitive to GSH. For this purpose, we chose the monomeric, bright, photostable and redox-insensitive protein mGold[18] to create a fusion with HT. This construct could also be targeted to specific organelles using established peptide localization sequences (Fig. 3a). To relate the TRaQ-G-mGold fluorescence ratio to a concentration of GSH, we expressed and purified the fusion protein HT-mGold and treated it with the TRaQ-G ligand. Mass spectrometry revealed that formation of the adduct is quantitative in vitro (Extended Data Fig. 3a). After purification, this adduct was used to generate a calibration curve, relating the ratio of mGold/TRaQ-G fluorescence intensities to GSH concentrations (Extended Data Fig. 3b). This ratiometric sensor responded linearly in the range of 1–20 mM GSH, confirming its suitability to quantify concentrations of GSH in the physiological range. The ratio is stable in the range between pH 6 and 9 (Supplementary Fig. 7). At pH 5, however, we observed precipitation of the protein, indicating that this sensor is not suitable for imaging GSH concentrations in acidic organelles such as lysosomes. Moreover, we recommend to generate calibration curves at the specific pH of the subcellular region of interest (ROI) because protonation of GSH affects its nucleophilicity.

To test the applicability of TRaQ-G in live-cell imaging, we generated a set of plasmids encoding for HT-mGold in the whole cell, calnexin–HT-mGold for endoplasmic reticulum (ER) targeting, H2B-HT-mGold for nuclear targeting, and ATP9-HT-mGold for targeting mitochondria (Methods). We transfected cells with these plasmids and compared the mGold signal to commercial markers of the respective subcellular region, revealing perfect overlap for the nucleus and the ER (Supplementary Fig. 8). In the case of mitochondria, we observed that, in some cells, the fusion protein is also present in the cytosol and nucleus (Supplementary Fig. 8). We excluded such cells from further analysis. Transfected cells were treated with 100 nM TRaQ-G ligand. With a short and simple incubation protocol, the sensor could be detected in the intended organelle with essentially no background signal (Fig. 3b–d). The ligands can also be used without washing. To image the ER, which has a more oxidizing environment than the cytosol[19], we also expressed a fusion of the redox-insensitive HT8[20]. Comparison of the redox-insensitive HT8 and the HT7 variant used for TRaQ-G indicated no measurable difference in binding efficiency or fluorogenicity (Supplementary Fig. 9a). We also measured the kinetics of labelling and found that intracellular labelling of HT is fast and reaches saturation in less than 30 min (Supplementary Fig. 9b). This experiment confirms that, under our imaging conditions, HT is stably labelled to its maximum extent. Furthermore, because the ligand does not have to be washed, newly expressed protein can continue to be labelled during long-term experiments.

Using TRaQ-G-mGold, we measured the equilibrium concentrations in the whole cell, the ER, the nucleus and mitochondria. The

concentration of GSH in the whole cell was ~18.9 ± 9.4 mM. This figure is not substantially different from those obtained using a commercial assay for cell lysates, which are 7.7–15.5 mM depending on the volume assumed for a HeLa cell (1,800–3,600 μm³)[21]. Importantly, we confirmed that overexpression of the fusion protein only altered GSH levels marginally. We noticed, however, that the transfection procedure that we used leads to a small but statistically significant increase in intracellular GSH (Supplementary Fig. 10). Thus, for a more accurate
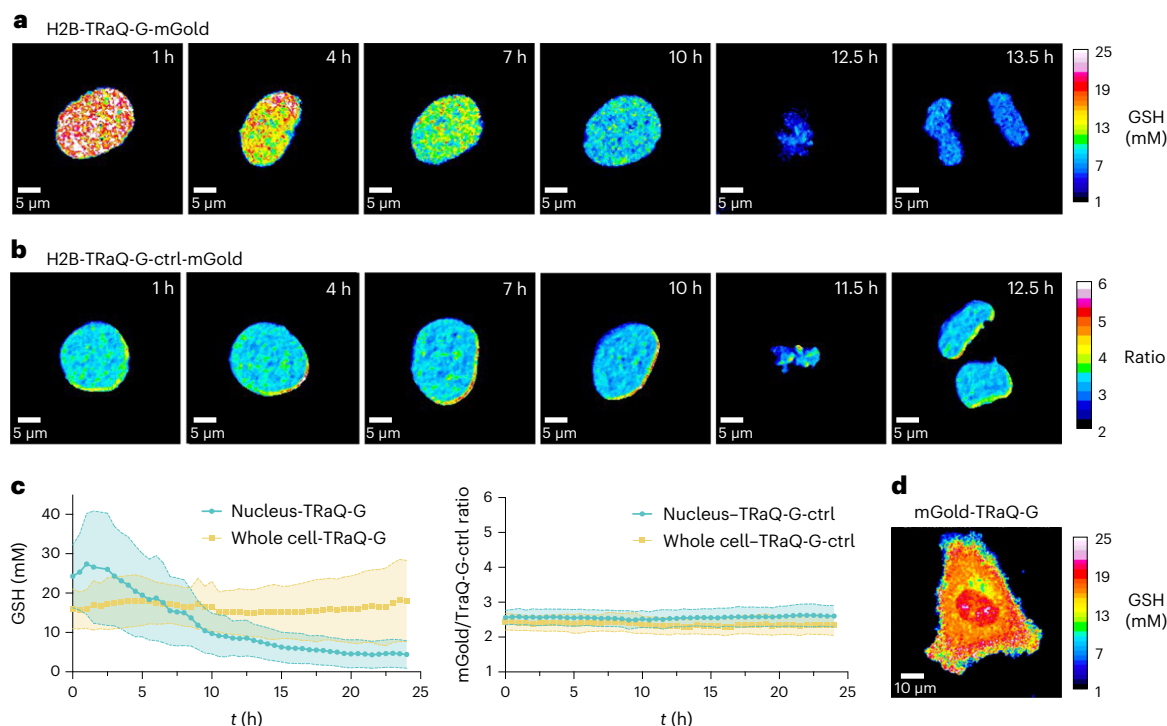
Fig. 3 | GSH quantification in subcellular locations using TRaQ-G-mGold.
a, Schematic depiction of the GSH sensor TRaQ-G-mGold with a targeting peptide and mechanism of ratiometric sensing. **b-d**, Ratiometric imaging of GSH in whole cells (**b**), ER (**c**) and nuclei (**d**) using TRaQ-G-mGold. **e,f**, GSH quantification in cells before (**e**) and 20 min after (**f**) the addition of 1 mM H_2O_2. **g**, Quantification of GSH concentration in whole cells, the ER or untreated nuclei (ctrl) after the addition of 10 mM EtGSH (membrane-permeant GSH precursor), 1 mM BSO (inhibitor of GSH biosynthesis) or 1 mM H_2O_2 (oxidant). The TRaQ-G ligand concentration was 100 nM in all cases. Images were generated by dividing the intensity of mGold over that of TRaQ-G and relating this ratio to the calibration curve obtained with purified TRaQ-G-mGold. For display purposes, calibrated images were despeckled using Fiji (ImageJ). Statistical significance was evaluated by one-way analysis of variance (ANOVA) (Šídák's multiple comparisons test) with $N = 132$, 142, 103, 127, 116, 129, 90, 118, 149, 176, 137 and 122 (from left to right) independent cells from three different passage numbers examined over three separate imaging sessions. Boxes represent 25th to 75th percentiles, the horizontal line represents the median, and whiskers extend from the minimum to the maximum.

Fig. 4 | Regulation of nuclear GSH concentrations during cell proliferation. **a**, H2B–TRaQ-G–mGold ratiometric imaging of a single nucleus from S phase to mitosis, revealing a steady decrease in GSH concentration. **b**, The control probe TRaQ-G-ctrl–mGold confirms that the observed variations are a consequence of GSH fluctuations. **c**, Quantification of GSH concentrations or the variation of the ratio with the control probe for 24 h after release of cells from thymidine block (early S phase). Lines represent average values, and the shaded areas represent the standard deviation from $N = 19, 50, 42$ and 19 independent cells from three different passage numbers examined over three separate imaging sessions, for H2B–TRaQ-G–mGold, H2B–TRaQ-G-ctrl–mGold, TRaQ-G–mGold and TRaQ-G-ctrl–mGold, respectively. **d**, TRaQ-G–mGold ratiometric imaging of a single cell ($t = 2$ h) displaying different concentrations in the nucleus and the rest of the cell.

determination of the absolute concentration, we recommend the development of gene-edited cell lines. Furthermore, flow-cytometry experiments demonstrated that overexpression did not influence the cellular levels of reactive oxygen species or induce concerning cytotoxicity (Supplementary Fig. 11 and Supplementary Table 3).

In the ER, a $[GSH + GSSG]_{ER}$ value of 19 ± 6 mM has been reported[19]. This value was obtained using a combination of Grx1-based sensors. Considering a GSH:GSSG ratio of 6:1 reported in the same study[19], a value of $[GSH]_{ER} = 14.3 \pm 4.5$ mM is obtained. This concentration is not significantly different from our own measurement of $[GSH]_{ER} = 9.2 \pm 5.3$ mM. In mitochondria, we found a GSH concentration of 4.8 ± 0.7 mM, which is in excellent agreement with the value obtained with sensor QG3.0 (4.4 ± 1.3 mM)[13]. As mentioned before, however, we noticed some cells in which the mitochondrial fusion protein could be observed in the cytoplasm and nucleus (Supplementary Fig. 8). Although these cells could be excluded from analysis, we decided to not pursue further experiments using these constructs. Finally, nuclei displayed GSH concentrations as high as 14.0 ± 6.7 mM. We observed substantial cell-to-cell variability in our GSH quantification experiments. These differences, in particular in the nuclear GSH pool, could be a consequence of cells being in different stages of the cell cycle[22]. This effect will be described in the next section.

Next, we tested whether mGold–TRaQ-G could be used to monitor changes in GSH concentration. For that purpose, we exposed cells equipped with the TRaQ-G–mGold sensor to reagents that would modify the intracellular GSH concentration (Fig. 3e–g and Supplementary Fig. 12). All three subcellular regions displayed higher GSH concentrations after treatment with glutathione monoethyl ester (EtGSH), a cell-permeable precursor of GSH (Fig. 3g). We hindered GSH biosynthesis by inhibiting γ-glutamylcysteine synthetase with buthionine sulfoximine (BSO), which led us to observe lower GSH

concentrations in the whole cell and the nucleus, but not in the ER, at least during our observation times (3–4 h post-treatment). Finally, cells treated with 1 mM H_2O_2 (20 min) also displayed a substantial decrease in GSH concentrations across organelles (Fig. 3e–g). Importantly, none of these treatments affected the fluorescence signal of the mGold protein (Supplementary Fig. 13), confirming its redox insensitivity.

Nuclear and cytosolic GSH pools are independently regulated
The high cell-to-cell variability observed in nuclear GSH concentrations led us to hypothesize that these differences could be correlated with the phase of the cell cycle. Although the existence of an independent nuclear GSH pool has been debated in the literature[9,23], there are indications that high GSH concentrations in the nucleus are required for cell proliferation and that the nuclear GSH pool varies during the cell cycle[22,23]. In particular, indirect evidence suggests that cells accumulate GSH in the nucleus in the S and G2 phases, before mitosis[22]. To test this hypothesis, we transfected HeLa cells with H2B–HT–mGold, synchronized them in the early S phase by double thymidine block[24], incubated them with either TRaQ-G ligand or the GSH-insensitive TRaQ-G-ctrl ligand, and imaged them for 24 h. Ratiometric imaging with H2B–TRaQ-G–mGold indicated that GSH concentration in the nucleus increased slightly in the first 1–2 h after thymidine block release, which corresponds to early S phase (Fig. 4a,c). After this time, GSH levels dropped steadily during the S phase, staying more or less stable through G2 phase and mitosis (Fig. 4a,c). We employed probe H2B–TRaQ-G-ctrl–mGold, which is insensitive to GSH (Fig. 2c), to demonstrate that these changes indeed reflect fluctuations in GSH concentration (Fig. 4b,c) and are not a consequence of photobleaching, changes in the expression levels of the sensor or other labelling artefacts.

Next, we tested whether the high GSH concentration in the S phase and subsequent decrease during the G2 phase were observed only in
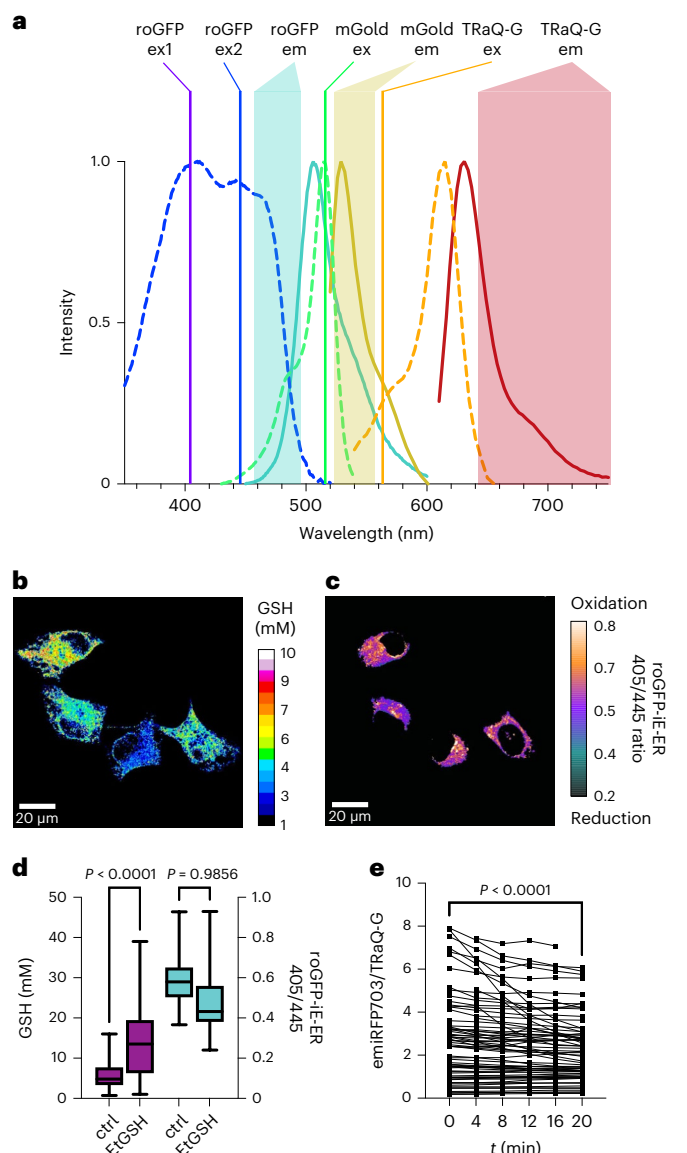
a

b

c

d

e

Fig. 5 | Multicolour and NIR imaging with TRaQ-G. a, Schematic representation of a four-colour experiment multiplexing roGFP-iE-ER and calnexin–TRaQ-G–mGold. Coloured lines represent the excitation wavelengths of the chromophores. Absorption (dashed lines) and emission spectra (solid lines) of the different fluorophores are displayed in corresponding colours, and shaded areas indicate the emission filters used to collect photons at different wavelengths. **b,c**, Ratiometric imaging of total GSH concentration using calnexin–TRaQ-G–mGold (**b**) and of redox potential (**c**) using roGFP-iE-ER. The image in **c** is not calibrated, and only the ratio of emission at 475 nm upon excitation at either 405 or 445 nm is displayed. **d**, Comparison of GSH concentrations and 405/445 ratios of roGFP-iE-ER in cells either untreated (ctrl) or after incubation with 10 mM EtGSH for 3 h. Statistical significance was evaluated by one-way ANOVA (Šídák's multiple comparisons test), for $N = 119, 115, 86, 103$ (from left to right) independent cells from three different passage numbers examined over three separate imaging sessions. **e**, Qualitative monitoring of the decrease in GSH concentration using the NIR sensor H2B–TRaQ-G-emiRFP703 (uncalibrated) in cells treated with 1 mM H_2O_2 during a period of 20 min. $N = 67$ independent cells per time point from three different passage numbers were examined over three separate imaging sessions. Statistical significance was evaluated by paired t-test. In **d**, boxes represent 25th to 75th percentiles, the centre line represents the median, and whiskers extend from minimum to maximum. In **e**, individual cell values are depicted.

the nucleus or in the whole cell. We transfected HeLa cells with HT–mGold and labelled them with either TRaQ-G or TRaQ-G-ctrl ligands. TRaQ-G imaging revealed that the GSH concentration in the whole

cell fluctuates substantially less than in the nucleus (Fig. 4c), and the concentration in the nucleus appears to be different to that in the rest of the cell (Fig. 4d). It should be noted that GSH fluctuations for the whole cell were heterogeneous between biological replicates, which may be a consequence of varying passage numbers or slightly different culture densities[7,22]; however, compartmentalization of nuclear GSH was observed in many cases. Finally, control experiments with TRaQ-G-ctrl in the whole cell indicated no noticeable variations in ratios between the nucleus or the rest of the cell throughout the experiment (Fig. 4c).

These findings indicate that the GSH concentration in the nucleus is regulated independently of that elsewhere in the cell, is highest during the S phase, and steadily decreases until mitosis. Furthermore, the existence of different GSH concentrations in the nucleus and the cytosol strongly implies that GSH does not diffuse freely across the nuclear envelope or through nuclear pores. These results also highlight the capabilities of our sensor, as differences between cytosolic and nuclear GSH pools could not be observed with other targetable sensors[9]. Further studies, beyond the scope of this work, will be required to determine the molecular mechanisms of GSH regulation in the nucleus.

Multicolour and near-infrared GSH imaging

We envisioned that TRaQ-G–mGold could be multiplexed with roGFPs to measure the total GSH concentration and the GSH/GSSG ratio simultaneously. roGFPs are ratiometric sensors that undergo an excitation wavelength shift from 405 to ~445 nm following reaction with GSSG[7,19]. Their emission wavelength is in both cases around 510 nm. Considering that mGold can be efficiently excited at 515 nm and its emission occurs around 570 nm, and TRaQ-G can be excited at 561 nm and emits at wavelengths beyond 600 nm, we planned the four-colour experiment depicted in Fig. 5a. Next, we co-transfected roGFP-iE-ER[19], a roGFP variant that has been engineered for the ER, and calnexin–TRaQ-G–mGold. Four-colour imaging showed that high GSH concentrations do not always correlate with a high GSH/GSSG ratio (Fig. 5b,c). This observation suggests that, even under conditions of high GSH accumulation, the concentration of GSSG also increases to maintain the redox potential. To test this hypothesis, we incubated cells with EtGSH, a membrane-permeant precursor of GSH. Using roGFP-iE-ER and calnexin–TRaQ-G–mGold, we observed that the concentration of GSH increases substantially, but the redox potential becomes only marginally more reductive (Fig. 5d). Although further experiments would be needed to understand this effect, these results demonstrate that TRaQ-G can be used in combination with roGFPs to study details of redox homeostasis in intracellular organelles.

Finally, the flexible design of TRaQ-G sensors allows for using a more redshifted fluorescence protein. To create a targeted GSH sensor reaching into the near-infrared (NIR) region of the spectrum, we created a plasmid encoding for an H2B–HT–emiRFP703[25] fusion protein. We transiently transfected HeLa cells with this construct, incubated them with 100 nM TRaQ-G and treated them with 1 mM H_2O_2. A drop in the emiRFP703/TRaQ-G ratio was observed corresponding to decreased GSH concentration (Fig. 5e). In particular, cells that had an initially high concentration (>4 emiRFP703/TRaQ-G) showed a more pronounced change. A reason for this behaviour could be that H_2O_2 does not oxidize GSH directly, but rather through the action of glutathione peroxidase[26]. This enzyme follows first-order kinetics with respect to GSH concentration, so the initial reaction rate varies linearly with GSH molarity[27]. This consideration explains why, under excess H_2O_2, cells with an initially higher GSH concentration display a faster GSH oxidation. However, additional studies would be necessary to validate these conclusions.

In conclusion, we have designed, synthesized and validated a new ratiometric GSH sensor, TRaQ-G, which only becomes reactive in the organelle of interest. This sensor is based on binding of a spirocyclic SiR ligand to HT, which induces isomerization to the GSH-sensitive and fluorescent zwitterionic form. We also created a GSH-insensitive control probe for validation studies. The availability of this control

probe is a key advantage of our sensor over existing probes, providing an excellent way to evaluate changes in redox homeostasis in live cells. We conducted X-ray diffraction experiments and MD simulations for structural elucidation of the different TRaQ-G adducts to gain mechanistic insight into the varying GSH sensitivities of the molecules. These data could also be used in future studies to improve the kinetics of our sensor by engineering the HT binding pocket, and more generally to design fluorogenic dyes or other robust, targeted sensors.

TRaQ-G–mGold was calibrated to measure the absolute GSH concentration of specific subcellular compartments in living cells. Our probe enabled the determination of GSH concentration in the whole cell and three other subcellular compartments, something that would have required four different probes or assays in the past. When the cellular GSH levels were artificially lowered or raised, TRaQ-G probes reliably detected changes in GSH concentration. We monitored the nuclear and overall GSH levels during cell division for over 24 h. The data suggest an independently regulated nuclear GSH pool and confirm that fluctuations of nuclear GSH are dependent on cell proliferation. Previous experiments using fractionated cell lysates pointed in this direction[22,23], but with TRaQ-G probes, it is now possible to monitor these changes in real time and with single-cell sensitivity. TRaQ-G is compatible with roGFP imaging for simultaneous imaging of absolute GSH concentration and organellar redox potential. Our sensor is spectrally flexible, and the FP can be exchanged for any colour complementary to the SiR-based ligand. In theory, it would even be possible to exchange the FP for another self-labelling tag to adapt the colour for any given experiment. In summary, we have presented a robust and flexible tool for live-cell GSH imaging that we used to observe the compartmentalization and fluctuation of cellular GSH. We believe that this concept could be extended to develop improved fluorescent sensors for other analytes.

Online content

Any methods, additional references, Nature Portfolio reporting summaries, source data, extended data, supplementary information, acknowledgements, peer review information; details of author contributions and competing interests; and statements of data and code availability are available at https://doi.org/10.1038/s41557-023-01249-3.

References

1. Meister, A. & Anderson, M. E. Glutathione. *Ann. Rev. Biochem.* **52**, 711–760 (1983).
2. Lushchak, V. I. Glutathione homeostasis and functions: potential targets for medical interventions. *J. Amino Acids* **2012**, e736837 (2012).
3. Montero, D., Tachibana, C., Rahr Winther, J. & Appenzeller-Herzog, C. Intracellular glutathione pools are heterogeneously concentrated. *Redox Biol.* **1**, 508–513 (2013).
4. Bansal, A. & Simon, M. C. Glutathione metabolism in cancer progression and treatment resistance. *J. Cell Biol.* **217**, 2291–2298 (2018).
5. Murakami, K. et al. Impairment of glutathione metabolism in erythrocytes from patients with diabetes mellitus. *Metabolism* **38**, 753–758 (1989).
6. Aoyama, K. & Nakaki, T. Impaired glutathione synthesis in neurodegeneration. *Int. J. Mol.* **14**, 21021–21044 (2013).
7. Gutscher, M. et al. Real-time imaging of the intracellular glutathione redox potential. *Nat. Methods* **5**, 553–559 (2008).
8. Hoseki, J., Oishi, A., Fujimura, T. & Sakai, Y. Development of a stable ERroGFP variant suitable for monitoring redox dynamics in the ER. *Biosci. Rep.* **36**, e00316 (2016).
9. Jiang, X. et al. Quantitative real-time imaging of glutathione with subcellular resolution. *Antioxid. Redox Signal.* **30**, 1900–1910 (2019).
10. Jiang, X. et al. Quantitative imaging of glutathione in live cells using a reversible reaction-based ratiometric fluorescent probe. *ACS Chem. Biol.* **10**, 864–874 (2015).
11. Jiang, X. et al. Quantitative real-time imaging of glutathione. *Nat. Commun.* **8**, 16087 (2017).
12. Jeong, E. M. et al. Real-time monitoring of glutathione in living cells reveals that high glutathione levels are required to maintain stem cell function. *Stem Cell Rep.* **10**, 600–614 (2018).
13. Umezawa, K., Yoshida, M., Kamiya, M., Yamasoba, T. & Urano, Y. Rational design of reversible fluorescent probes for live-cell imaging and quantification of fast glutathione dynamics. *Nat. Chem.* **9**, 279–286 (2017).
14. Lukinavičius, G. et al. A near-infrared fluorophore for live-cell super-resolution microscopy of cellular proteins. *Nat. Chem.* **5**, 132–139 (2013).
15. Grimm, J. B. et al. A general method to fine-tune fluorophores for live-cell and in vivo imaging. *Nat. Methods* **14**, 987–994 (2017).
16. Wang, L. et al. A general strategy to develop cell permeable and fluorogenic probes for multicolour nanoscopy. *Nat. Chem.* **12**, 165–172 (2020).
17. Frei, M. S. et al. Engineered HaloTag variants for fluorescence lifetime multiplexing. *Nat. Methods* **19**, 65–70 (2022).
18. Lee, J. et al. Versatile phenotype-activated cell sorting. *Sci. Adv.* **6**, eabb7438 (2020).
19. Birk, J. et al. Endoplasmic reticulum: reduced and oxidized glutathione revisited. *J. Cell Sci.* **126**, 1604–1617 (2013).
20. Deprey, K. & Kritzer, J. A. HaloTag forms an intramolecular disulfide. *Bioconjugate Chem.* **32**, 964–970 (2021).
21. Cadart, C., Venkova, L., Piel, M. & Cosentino Lagomarsino, M. Volume growth in animal cells is cell cycle dependent and shows additive fluctuations. *eLife* **11**, e70816 (2022).
22. Markovic, J. et al. Glutathione is recruited into the nucleus in early phases of cell proliferation. *J. Biol. Chem.* **282**, 20416–20424 (2007).
23. García-Giménez, J. L. et al. Nuclear glutathione. *Biochim. Biophys. Acta* **1830**, 3304–3316 (2013).
24. Chen, G. & Deng, X. Cell synchronization by double thymidine block. *Bio Protoc.* **8**, e2994 (2018).
25. Matlashov, M. E. et al. A set of monomeric near-infrared fluorescent proteins for multicolor imaging across scales. *Nat. Commun.* **11**, 239 (2020).
26. Lubos, E., Loscalzo, J. & Handy, D. E. Glutathione peroxidase-1 in health and disease: from molecular mechanisms to therapeutic opportunities. *Antioxid. Redox Signal.* **15**, 1957–1997 (2011).
27. Brand, L. & Floh, A. Kinetics of glutathione peroxidase. *Biochim. Biophys. Acta* **191**, 541–549 (1969).

Methods

Optical spectroscopic methods

Stock solutions were prepared in DMSO (spectrophotometric grade >99.9%) at concentrations of 50 mM and stored at −20 °C. UV–vis spectra were acquired using a Multiskan SkyHigh microplate spectrophotometer (ThermoFisher Scientific) and 96-well plates (Corning) or quartz cuvettes using SkanIt software. Fluorescence spectra were acquired using an FS5 spectrofluorometer (Edinburgh Instruments) equipped with an SC-40 plate reader and 96-well plates (Corning) using Fluoracle software. The obtained spectra were background-corrected.

Quantum yields were measured at concentrations of 1–10 μM depending on the brightness of the respective molecule, using an SC-30 integrating sphere and quartz cuvettes. Extinction coefficients were measured by creating a dilution series (1–15 μM), measuring the absorbance at λ_{max} and applying a linear regression. Measurements for the turn-on ligands were performed at pH 2 to enhance the zwitterionic form as much as possible. Extinction coefficients of HT adducts were measured in the presence of a twofold excess of HT protein to ensure quantitative reaction of the ligand.

All measurements were carried out as three technical replicates and at 20 °C unless stated otherwise.

Cloning

Primers for Gibson assembly were designed using SnapGene (version 4.1.9). Respective precursor plasmids and primers are reported in Supplementary Tables 4 and 5. Reagents and general procedures from the Gibson assembly cloning kit from New England Biolabs (NEB) were used. Vector and insert fragments were linearized by polymerase chain reaction (PCR) and template DNA was digested with DpnI. PCR fragments were purified with the QIAquick PCR purification kit from Qiagen. Backbone and insert fragment were ligated and transformed by heat shock into NEB 5α competent cells following the provided standard procedure of the vendor. Plasmids were amplified by incubation of lysogeny broth (LB) cultures containing the appropriate antibiotics overnight at 37 °C. DNA was isolated using the Qiagen Plasmid Mini kit or the Qiagen Plasmid Plus Midi kit. The correct sequence of the gene of interest (GOI) was confirmed by the Sanger sequencing service of Microsynth. New constructs reported in this Article are available from Addgene: H2B–HT–emiRFP703 (183985), HT–mGold (183986), calnexin–HT–mGold (183987), H2B–HT–mGold (183988) and calnexin–HT8–mGold (183989).

Site-directed mutagenesis

Primers for site-directed mutagenesis were designed with NEBaseChanger. The respective precursor plasmids and primers are reported in Supplementary Tables 4 and 5. The standard procedure and reagents from the Q5 Site-Directed Mutagenesis kit (NEB) were used to insert mutations, ligate plasmids and transform them into NEB 5α competent cells by heat shock. The correct sequence of the GOI was confirmed by the Sanger sequencing service of Microsynth.

Protein expression

BL21(DE3) competent cells from NEB were transformed with the respective plasmid by heat shock following the provided standard procedure of the vendor. LB medium was prepared with the appropriate antibiotic. A single colony was inoculated into 100 ml of LB medium containing the appropriate antibiotics and incubated at 37 °C overnight. A 20-ml volume of the starter culture was inoculated into 1 l of medium and incubated at 37 °C until an optical density of 0.4–0.8 was reached. Isopropyl β-D-1-thiogalactopyranoside (IPTG) was added to a final concentration of 1 mM and the culture was further incubated at 18 °C overnight. *Escherichia coli* were harvested by centrifugation and resuspended in HEPES buffer (20 mM HEPES, 300 mM NaCl, pH 7.4). Glycerol was added to a final concentration of 10% as well as turbonuclease (5 μl) and a protease inhibitor cocktail tablet (Roche). The cells were lysed by sonication (70% amplitude, 10-s pulse on/10-s pulse off for 2.5 min). The lysate was cleared

by centrifugation and the protein was purified by Ni-His-affinity chromatography in batch mode. Fractions were analysed by gel electrophoresis, and pure fractions were pooled and dialysed against PBS.

Protein crystallization and structural analysis

HT protein (~1 mg ml⁻¹) was reacted with the respective ligand (1.5× excess) in PBS at 20 °C for 1 h. The adduct was purified by size-exclusion chromatography and concentrated to ~10 mg ml⁻¹. The adducts were screened by the sitting-drop vapour diffusion method using commercially available screens from Molecular Dimensions and Qiagen, dispensed by the Mosquito robot (TTP Labtech). Crystals of HT adducts formed in a couple of days in 25% vol/vol PEG smear medium and 0.1 M Tris pH 8.5 (Me–TRaQ-G), in 20% vol/vol PEG 6000, 10% ethylene glycol, 0.1 M magnesium chloride hexahydrate and 0.1 M MES pH 6 (TRaQ-G) and in 20% vol/vol PEG 6000, 0.1 M lithium chloride and 0.1 M sodium citrate pH 4 (TRaQ-G-ctrl). The crystals were cryoprotected with 25% glycerol. Diffraction data were collected at the Paul Scherrer Institute (Swiss Light Source, Villigen) at the PXIII beamline. Data were processed with the XDS program package[28]. Structures were solved by molecular replacement using Phaser-MR and chain A of PDB 6U32 as the model. Manual model building and structure refinement were carried out with PHENIX (version 1.20.1-4487)[29], Coot (version 0.9.6)[30] and phenix-refine, respectively. After validation, the structures of the HaloTag adducts were deposited in the PDB database under PDB codes 7ZBA (Me–TRaQ-G), 7ZBB (TRaQ-G-ctrl) and 7ZBD (TRaQ-G). Data collection and refinement statistics are summarized in Supplementary Table 6. Depictions of adduct structures were generated using PyMOL (version 2.4.0)[31].

Molecular dynamics simulations

Atomistic MD simulations were performed starting from the crystal structures of HT with the closed and open form of the TRaQ-G probe, as well as with Me–TRaQ-G and TRaQ-G-ctrl probes. All MD simulations were performed with the program package GROMACS (version 2020.4)[32] using the GROMOS 54a7 force field[33]. The ligand parameters were obtained from Automated Topology Builder[34,35].

The ligands were bound to D106 according to the crystal structures using the [intermolecular_interactions] block of GROMACS with a bond length of 0.185 nm, a force constant of 10^5 kJ mol⁻¹ nm⁻² and bond type 6. The proteins were neutralized and solvated in 0.15 M NaCl solution using the simple point-charge water model and a box size of $7.0 \times 7.0 \times 7.0$ nm³. After a steepest descent minimization (5,000 steps), the systems were equilibrated in several steps ((1) 500-ps simulation with constant number of particles, volume and temperature, and with a time step of $\Delta t = 0.5$ fs; (2) 1-ns simulation with constant number of particles, pressure and temperature (NPT), and with $\Delta t = 1$ fs; (3) 1-ns NPT simulation with $\Delta t = 1$ fs; (4) 1-ns NPT simulation with $\Delta t = 2$ fs). During the first two equilibration steps, position restraints were applied to the protein. The production simulations were performed for 500 ns using a time step of $\Delta t = 2$ fs. The temperature was kept at 300 K in all simulations using a velocity rescaling thermostat[36], and the pressure was kept at 1 bar (using a Berendsen barostat[37] for the equilibration steps and a Parrinello–Rahman barostat[38] for the production). All bond lengths were constraint using the linear constraint solver (LINCS) algorithm[39]. Van der Waals interactions were treated with a cutoff scheme. Coulomb interactions were calculated using the particle-mesh Ewald (PME) algorithm. Analyses were performed using GROMACS tools.

In addition, simulations of the GSH adducts of TRaQ-G and Me–TRaQ-G were performed following the protocol described above. The starting conformations were obtained by manually binding GS(H) to a snapshot of the MD simulation of TRaQ-G and the crystal structure of Me–TRaQ-G, respectively.

In vitro GSH sensitivity and selectivity experiments

The HT adducts were prepared by combining the HT protein (~50 μM in PBS) with the respective TRaQ-G ligand (1.5–2× excess, stock solution

50 mM in DMSO) and rotating the resulting solution for 1 h at 20 °C. The adduct was further concentrated, and excess TRaQ-G ligand was removed by desalting with Zeba spin desalting columns (7k molecular weight cutoff, 0.5 ml). The product was diluted with 0.5 M sodium phosphate buffer to a final concentration of ~5–15 μM. In a 96-well plate, the adduct solution was treated with the appropriate amount of an aqueous stock solution of GSH, GSSG, cysteine, H_2S or taurine, and the solutions were incubated at 20 °C for 30–60 min. Absorbance at 615 nm and/or fluorescence at 630 nm were measured in triplicates, including separate blanks for every concentration of the reagents.

pH profile

Adduct of purified HT–mGold fusion protein with TRaQ-G ligand (20 μM) was added to buffers of pH 2–13 (pH 2, citric acid; pH 3–7, citric acid/disodium hydrogen phosphate; pH 8, disodium hydrogen phosphate; pH 9–11, sodium hydrogencarbonate/disodium carbonate; pH 12–13, KCl/NaOH), and fluorescence spectra were measured. The ratio between mGold and the SiR fluorescence at λ_{max} was calculated. At pH < 5 the protein precipitated, and at pH > 9 the mGold fluorescence dropped dramatically. The ratio is stable between pH 6 and 9, but separate calibration curves for every specific pH are recommended as the protonation state of GSH changes.

Kinetics measurements

The HT adducts were prepared as described previously. A final concentration of ~15 μM adduct was used for the measurements. In a 96-well plate, GSH was added (final concentration of 5 mM) to the adduct solution and the measurement loop was started. Absorbance was measured in triplicates including a blank measurement without adduct present. After equilibration was reached, N-ethylmaleimide (NEM, final concentration 40 mM) or iodoacetamide (final concentration 50 mM) were added and a second measurement loop was started. For Me–TRaQ-G the measurement was carried out at 20 °C, and for TRaQ-G the measurement was carried out at 37 °C.

Calibration curve

The TRaQ-G sensor was assembled in vitro as described before using the purified HT–mGold fusion protein. The adduct was used in a final concentration of 10 μM. In a 96-well plate, the adduct was treated with the appropriate amount of GSH. The mGold/SiR ratio was measured by fluorescence microscopy. The ratiometric measurement was carried out with the same instrument with the same settings as for all other measurements. The measurement was performed in three technical replicates and the blank averaged over all concentrations. Three fields of view (FOVs) were measured per well. Image analysis was performed with Fiji (ImageJ). The background was determined from the blank measurements, calculating the mean of all the pixels in the FOV per channel, excluding the edges. The background was subtracted for the sample measurements and each channel. The mGold channel was divided by the SiR channel in a pixel-by-pixel manner, and the mean of all pixels in the FOV, excluding the edges, was calculated. Every FOV gave one data point.

Cell culture

HeLa cells were grown in DMEM supplemented with fetal bovine serum (FBS, 10%) and penicillin (100 U ml^{-1})/streptomycin (100 μg ml^{-1})/fungizone (0.25 μg ml^{-1}) at 37 °C in a 5% CO_2 environment. For imaging, 15,000–20,000 cells were seeded per well on an eight-well Ibidi chambered cover glass two to three days before imaging. If required, cells were transfected with plasmid DNA using jetPRIME according to the recommended protocol of the supplier, one to two days before imaging. The cells were incubated with the respective probes in growth medium for the indicated time. Before imaging, the growth medium was removed, then the cells were washed with PBS (2×) and imaged in FluoroBrite DMEM.

Flow cytometry

HeLa cells were transfected >24 h before the measurement with HT–mGold, if applicable. Cells were incubated with 1 μM CellRox DeepRed at 37 °C for 1 h and detached by trypsination. The positive control was treated with 1 mM tert-butyl hydrogenperoxide at 37 °C for 1 h. The cells were then collected by centrifugation, washed with cold PBS and incubated with annexinV-Pacific Blue in annexin-binding buffer at 20 °C for 15 min. Samples were filtered through cell strainer tubes and analysed by a FACS Canto II system equipped with 405-nm, 448-nm and 633-nm laser lines. Data were analysed using FlowJo (v9) software.

Confocal microscopy

Confocal imaging was performed with a dual-camera Nikon W1 spinning disc microscope equipped with an sCMOS camera (Photometrix). Bright-field imaging was performed with a white light-emitting diode. Laser lines and filters were set up for the appropriate channels as described in Supplementary Table 7. Images were collected using a CFI Plan Apochromat Lambda D oil immersion objective (×60, NA = 1.4) and for roGFP imaging a CFI Plan Apo VC water immersion objective (×60, NA = 1.2). Channels were imaged sequentially. The microscope was operated using NIS-Elements software. Imaging was performed at 37 °C in a 5% CO_2 environment.

Image analysis

The background was determined by manually picking regions without cells or with untransfected cells. The mean background value for each channel was further used in automated image analysis. Ratiometric image analysis was conducted using a Python script (available from https://gitlab.uzh.ch/locbp/public/ratiometric-image-analysis). The background was subtracted for each channel and the ROIs (=transfected cells) were determined by thresholding or with the Cellpose[40] algorithm in the channel of the FP. To obtain ratiometric images, the masks were applied to the background-subtracted images and the FP channel was divided by the SiR channel in a pixel-by-pixel manner within the ROIs. Single cells were either identified by selecting coherent regions in a certain range of size or by using the ROIs earlier defined by Cellpose. For measurements with ATP9–HT–mGold, cells with appropriate localization of the sensor and segmentation of mitochondria were selected manually from the ratiometric images. The mean of all ratiometric pixels per cell was calculated and represents one data point. Cells from all replicates were combined for further analyses. The statistical analyses were performed using Prism9 GraphPad and generally included a ROUT outlier analysis. Calculated values are always given as mean ± standard deviation. Additionally, our linear calibration equation was applied to the ratiometric images and saved for each FOV. For display only, images were despeckled with Fiji (ImageJ).

GSH measurement in living HeLa cells

HeLa cells were plated and transfected with the respective HT–mGold plasmid. After 24–48 h, the cells were incubated with 100 nM TRaQ-G ligand for 1 h. The cells were treated with 10 mM EtGSH in FluoroBrite DMEM for 3–4 h, 1 mM BSO in FluoroBrite DMEM for 3–4 h, 1 mM H_2O_2 for 20 min in FluoroBrite or vehicle (FluoroBrite DMEM). GSH concentration was measured by fluorescence microscopy using the calibration curve. The experiment was carried out in three biological replicates on different days with cells from different passages. The datasets were combined for analysis. In total, 90–176 cells were analysed per condition. The calibration curve was used to interpolate/extrapolate means as well as the upper and lower bounds, expressed in GSH concentration for single cells.

GSH measurement with a commercial GSH assay

HeLa cells were plated in T75 flasks, grown for two to three days and transfected with HT–mGold, HT–mGold-His6 plasmid for expression

in *E. coli* or left untreated. The T7 promotor in the control plasmid should not lead to protein expression in mammalian cells. After 24 h cells were collected by trypsination, counted, and washed with cold PBS. 5 million cells were used for the GSH assay after lysing by sonication (20 kHz, 70% amplitude, 2 × 10 s). The standard procedure of the kit (Sigma-Aldrich, MAK364) was followed to determine the total amount of reduced GSH in all samples. The experiment was performed in three biological replicates. The total amount of GSH was used to estimate the intracellular GSH concentration. For HeLa cells a volume of 1,800–3,600 µm³ per cell can be assumed[21], yielding an intracellular GSH concentration of 7.7–15.5 mM.

GSH measurement during cell proliferation

HeLa cells were plated and transfected with the HT–mGold or H2B–HT–mGold plasmid. About 8 h after transfection, thymidine (100 mM aqueous stock solution, final concentration 2 mM) was added to the cells and incubated for 16 h. The cells were washed with PBS and incubated in fresh medium for 9 h. Thymidine was added again (final concentration 2 mM) and incubated for 18 h. Before imaging, the cells were incubated with 100 nM TRaQ-G or TRaQ-G-ctrl ligand for 1 h in culture medium still containing thymidine. Cells were imaged in fresh FluoroBrite DMEM supplemented with 4 mM glutamine, 1 mM sodium pyruvate, 10% FBS and penicillin (100 U ml⁻¹)/streptomycin (100 µg ml⁻¹)/fungizone (0.25 µg ml⁻¹). Frames were taken every 30 min over 24 h. For analysis, ratiometric images of the whole FOV were generated with the method described before. From each FOV, the dividing cells were segmented and followed over time by hand. The mean of all pixels within one cell represents one data point. The experiment was carried out in three biological replicates on different days with cells from different passages. The datasets were combined for analysis. In total, a minimum of 19 cells were analysed per condition and frame. The calibration curve was used to interpolate/extrapolate means as well as upper and lower bounds expressed in GSH concentration per time point.

Four-colour imaging with TRaQ-G and roGFP

HeLa cells were plated and co-transfected with ER–Halo–mGold and roGFP-iE-ER (3:1). After 24–48 h, the cells were incubated with the TRaQ-G ligand for 1 h. The cells were treated with 10 mM EtGSH in FluoroBrite DMEM for 3–4 h or vehicle (FluoroBrite DMEM). The same cells were imaged with the ×60 oil immersion objective for GSH concentration and the ×60 water immersion objective for the redox potential. The experiment was carried out in three biological replicates on different days, with cells from different passages. The datasets were combined for analysis. In total, 86–119 cells were imaged per condition. The calibration curve was used to interpolate/extrapolate means as well as upper and lower bounds expressed in GSH concentration for single cells.

Reporting summary

Further information on research design is available in the Nature Portfolio Reporting Summary linked to this Article.

Data availability

X-ray crystallographic data are available from the PDB under accession numbers 6U32 (reference), 7ZBA, 7ZBB and 7ZBD. All other data are available on Zenodo at https://doi.org/10.5281/zenodo.6412450. Source data are provided with this paper.

Code availability

Python scripts for automated image analysis are available on https://gitlab.uzh.ch/locbp/public/ratiometric-image-analysis.

References

28. Kabsch, W. XDS. *Acta Crystallogr. D Biol. Crystallogr.* **66**, 125–132 (2010).

29. Liebschner, D. et al. Macromolecular structure determination using X-rays, neutrons and electrons: recent developments in Phenix. *Acta Crystallogr. D Struct. Biol.* **75**, 861–877 (2019).

30. Emsley, P., Lohkamp, B., Scott, W. G. & Cowtan, K. Features and development of Coot. *Acta Crystallogr. D Biol. Crystallogr.* **66**, 486–501 (2010).

31. Schrödinger, L. L. C. The PyMOL Molecular Graphics System, Version 1.8 (2015).

32. Abraham, M. J. et al. GROMACS: high performance molecular simulations through multi-level parallelism from laptops to supercomputers. *SoftwareX* **1–2**, 19–25 (2015).

33. Schmid, N. et al. Definition and testing of the GROMOS force-field versions 54A7 and 54B7. *Eur. Biophys. J.* **40**, 843–856 (2011).

34. Malde, A. K. et al. An automated force field topology builder (ATB) and repository: version 1.0. *J. Chem. Theory Comput.* **7**, 4026–4037 (2011).

35. Stroet, M. et al. Automated topology builder Version 3.0: prediction of solvation free enthalpies in water and hexane. *J. Chem. Theory Comput.* **14**, 5834–5845 (2018).

36. Bussi, G., Donadio, D. & Parrinello, M. Canonical sampling through velocity rescaling. *J. Chem. Phys.* **126**, 014101 (2007).

37. Berendsen, H. J. C., Postma, J. P. M., van Gunsteren, W. F., DiNola, A. & Haak, J. R. Molecular dynamics with coupling to an external bath. *J. Chem. Phys.* **81**, 3684–3690 (1984).

38. Parrinello, M. & Rahman, A. Polymorphic transitions in single crystals: a new molecular dynamics method. *J. Appl. Phys.* **52**, 7182–7190 (1981).

39. Hess, B. P-LINCS: a parallel linear constraint solver for molecular simulation. *J. Chem. Theory Comput.* **4**, 116–122 (2008).

40. Stringer, C., Wang, T., Michaelos, M. & Pachitariu, M. Cellpose: a generalist algorithm for cellular segmentation. *Nat. Methods* **18**, 100–106 (2021).

Author contributions

S.E. and P.R.-F. conceived the project. S.E. performed the synthesis of small molecules, cloning of plasmids, protein expression and purification, titrations, kinetics experiments, X-ray diffraction analyses, cell culture, imaging, data analysis and manuscript preparation. G.Q. contributed to the synthesis of TRaQ-G-ctrl, to cloning of some plasmids, and to image acquisition and analysis. S.T. performed and analysed MD simulations. P.R.-F. supervised the project and contributed to data analysis and manuscript preparation.

Competing interests

The authors declare no competing interests.
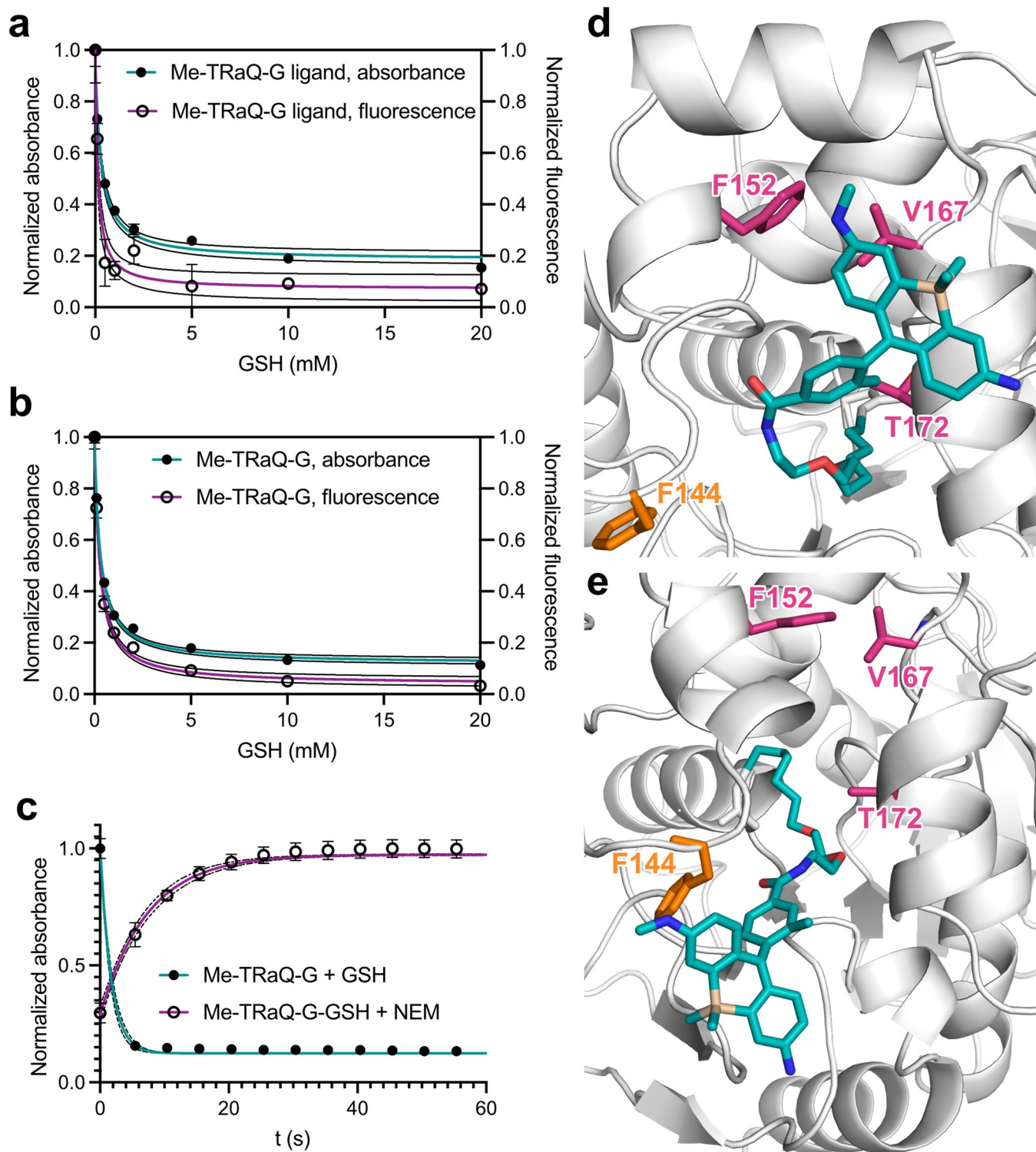
Additional information

Extended data is available for this paper at
https://doi.org/10.1038/s41557-023-01249-3.

Extended Data Fig. 1 | GSH titrations and MD results. a) Me–TRaQ-G shows good GSH-sensitivity in the range of 0–5 mM by itself and **b)** as HT adduct. **c)** The conjugate with GSH forms rapidly in vitro and is reversible by adding the GSH scavenger NEM. $N = 3$ independently prepared samples examined over 3 independent measurements. Data are presented as mean values and error bars indicate the standard deviation. Data were fitted by one-phase decay, dotted lines represent 95% confidence interval (CI). **d)** Preferred conformation of Me–TRaQ-G during MD simulation (322 ns) with methyl group pointing into hydrophobic pocket. **e)** Short-lived conformation of Me–TRaQ-G during MD simulation (457 ns) with methyl group exposed to the solvent. Residues forming the hydrophobic pocket are displayed in pink, the Phe residue that moves between the open and closed conformation is displayed in orange.
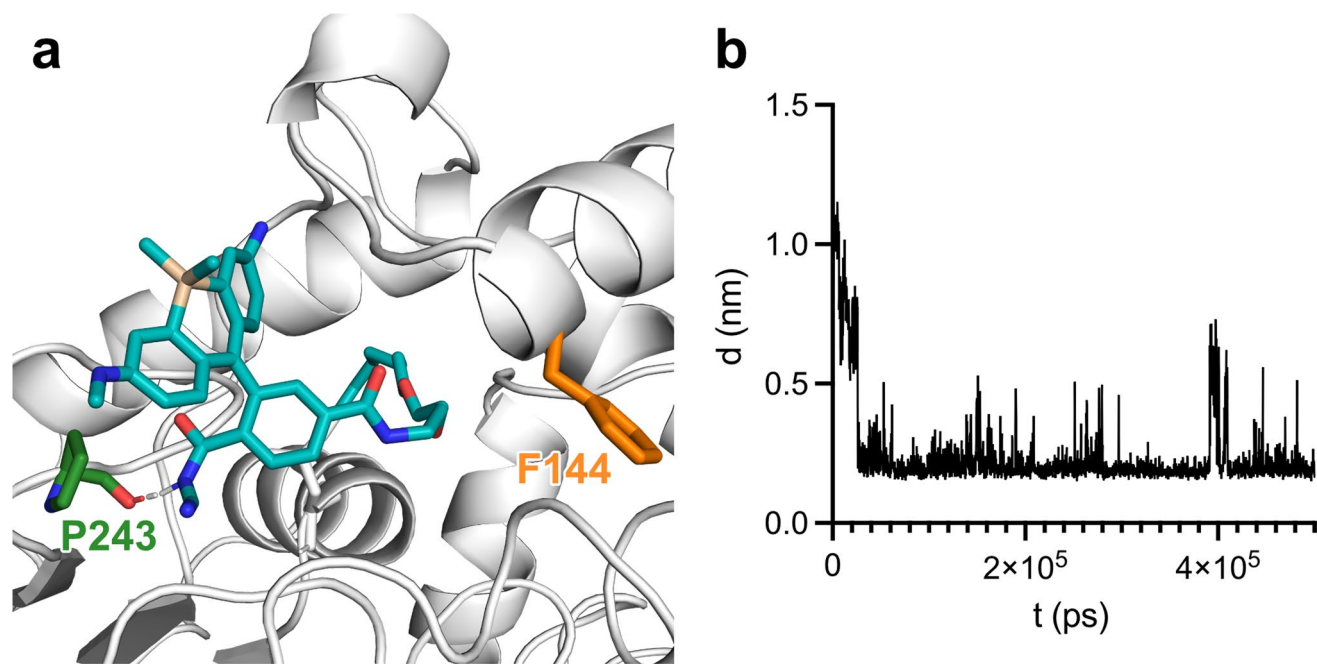
Extended Data Fig. 2 | Hydrogen bonding in TRaQ-G. a) Snapshot during MD simulation of open TRaQ-G at 102 ns. **b)** Length of the hydrogen bond between the cyanamide proton and the backbone carbonyl of P243 during the simulation. The Phe residue that moves between the open and closed conformation is displayed in orange and the residue forming a hydrogen bond with the ligand is displayed in green.

a

b
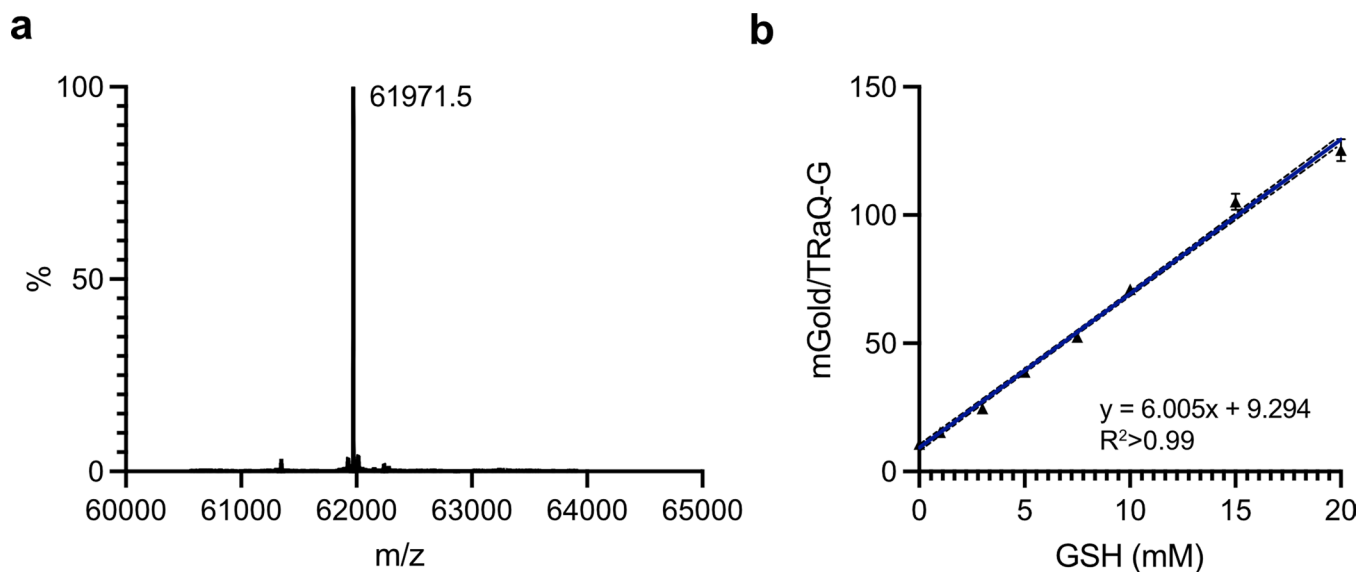
Extended Data Fig. 3 | In vitro characterization and calibration of TraQ-G.
a) Deconvoluted mass spectrum of TRaQ-G reacted with HT *in vitro*.
b) Calibration curve of TRaQ-G with adduct formed by *in vitro* reaction of purified fusion protein with ligand and measured by fluorescence microscopy. *N* = 3 independently prepared samples examined over 3 independent measurements. Data are presented as mean values and error bars indicate the standard deviation. Data were fitted by linear regression. Dashed line represents 95% CI.

nature portfolio

Corresponding author(s):   Pablo Rivera-Fuentes

Last updated by author(s):   April 6, 2023

Reporting Summary

Nature Portfolio wishes to improve the reproducibility of the work that we publish. This form provides structure for consistency and transparency in reporting. For further information on Nature Portfolio policies, see our Editorial Policies and the Editorial Policy Checklist.

Statistics

For all statistical analyses, confirm that the following items are present in the figure legend, table legend, main text, or Methods section.

n/a	Confirmed	
☐	☒	The exact sample size (n) for each experimental group/condition, given as a discrete number and unit of measurement
☐	☒	A statement on whether measurements were taken from distinct samples or whether the same sample was measured repeatedly
☐	☒	The statistical test(s) used AND whether they are one- or two-sided *Only common tests should be described solely by name; describe more complex techniques in the Methods section.*
☐	☒	A description of all covariates tested
☐	☒	A description of any assumptions or corrections, such as tests of normality and adjustment for multiple comparisons
☐	☒	A full description of the statistical parameters including central tendency (e.g. means) or other basic estimates (e.g. regression coefficient) AND variation (e.g. standard deviation) or associated estimates of uncertainty (e.g. confidence intervals)
☐	☒	For null hypothesis testing, the test statistic (e.g. F, t, r) with confidence intervals, effect sizes, degrees of freedom and P value noted *Give P values as exact values whenever suitable.*
☒	☐	For Bayesian analysis, information on the choice of priors and Markov chain Monte Carlo settings
☒	☐	For hierarchical and complex designs, identification of the appropriate level for tests and full reporting of outcomes
☒	☐	Estimates of effect sizes (e.g. Cohen's d, Pearson's r), indicating how they were calculated

Our web collection on statistics for biologists contains articles on many of the points above.

Software and code

Policy information about availability of computer code

Data collection	Imaging: NIS-Elements AR; UV/Vis spectroscopy: SkanIt, Fluoracle; NMR: TopSpin (4.2.0).
Data analysis	Imaging: Fiji, custom python script (https://gitlab.uzh.ch/locbp/public/ratiometric-image-analysis). Statistical analysis: Prism 9. Crystallography: XDS (2022), Phenix (1.20.1-4487), Coot (0.9.6), PyMOL (2.4.0). Sequencing: SnapGene (4.1.9). NMR: MestReNova (14.2). Molecular dynamics: GROMACS (2020.4) Flow cytometry: FACEDiva (6.1.3) FlowJo v9

For manuscripts utilizing custom algorithms or software that are central to the research but not yet described in published literature, software must be made available to editors and reviewers. We strongly encourage code deposition in a community repository (e.g. GitHub). See the Nature Portfolio guidelines for submitting code & software for further information.

Data

Policy information about availability of data

All manuscripts must include a data availability statement. This statement should provide the following information, where applicable:

- Accession codes, unique identifiers, or web links for publicly available datasets
- A description of any restrictions on data availability
- For clinical datasets or third party data, please ensure that the statement adheres to our policy

X-ray crystallographic data are available from the PDB under accession numbers 6U32 (reference), 7ZBA, 7ZBB, and 7ZBD. All other data are available on Zenodo with the following DOI: 10.5281/zenodo.6412450

Field-specific reporting

Please select the one below that is the best fit for your research. If you are not sure, read the appropriate sections before making your selection.

☒ Life sciences   ☐ Behavioural & social sciences   ☐ Ecological, evolutionary & environmental sciences

For a reference copy of the document with all sections, see nature.com/documents/nr-reporting-summary-flat.pdf

Life sciences study design

All studies must disclose on these points even when the disclosure is negative.

Sample size	No statistical methods were used to determine the sample size, but rather we followed common practices in previously reported studies. For each condition of each replicate, five field of views were imaged. The sample size was defined by the number of healthy, transfected cells in each field of view.
Data exclusions	In general, a standard outlier analysis (ROUT, Q=1%) was performed. In the cell cycle imaging with TRaQ-G in the nucleus, the 2 h timepoint was retrospectively omitted as many fields of view were out of focus.
Replication	All experiments that included living cells were performed in biological triplicates on different days with cells of different passages. UV/Vis experiments for the characterization of the sensor were performed in technical triplicates. All attempts at replication were successful.
Randomization	Regions of interest for live cells imaging were selected at random. Cells for toxicity or GSH experiments were also selected randomly. Aliquots of probes and purified protein were also randomly selected for in vitro studies.
Blinding	Researchers were not blinded to group allocation. We since all analyses were performed in an automated way, the researcher could not influence the outcome of the analysis even if they know to which group the sample belongs.

Reporting for specific materials, systems and methods

We require information from authors about some types of materials, experimental systems and methods used in many studies. Here, indicate whether each material, system or method listed is relevant to your study. If you are not sure if a list item applies to your research, read the appropriate section before selecting a response.

Materials & experimental systems

n/a	Involved in the study
☒	☐ Antibodies
☐	☒ Eukaryotic cell lines
☒	☐ Palaeontology and archaeology
☒	☐ Animals and other organisms
☒	☐ Human research participants
☒	☐ Clinical data
☒	☐ Dual use research of concern

Methods

n/a	Involved in the study
☒	☐ ChIP-seq
☐	☒ Flow cytometry
☒	☐ MRI-based neuroimaging

Eukaryotic cell lines

Policy information about cell lines

Cell line source(s)	HeLa (CLS Cell Line Service GmbH)
Authentication	Cell lines were not authenticated.

| Mycoplasma contamination | Cell lines were not tested for mycoplamsa contamination. |
| Commonly misidentified lines (See ICLAC register) | No commonly misidentified cell lines were used. |

Flow Cytometry

Plots

Confirm that:

☒ The axis labels state the marker and fluorochrome used (e.g. CD4-FITC).

☐ The axis scales are clearly visible. Include numbers along axes only for bottom left plot of group (a 'group' is an analysis of identical markers).

☐ All plots are contour plots with outliers or pseudocolor plots.

☒ A numerical value for number of cells or percentage (with statistics) is provided.

Methodology

Sample preparation	HeLa cells were transfected >24 h before the measurement, if applicable. Cells were detached by trypsination and harvested by centrifugation, washed with cold PBS and filtered through cell strainer tubes. Transfection, treatment and staining was performed depending on the experiment as stated in the method section.
Instrument	FACS Canto II
Software	Data were collected with FACSDiva (6.1.3) and recorded data were analyzed with FlowJo v9.
Cell population abundance	Population sizes are mentioned at the appropriate place in the Supplementary Information.
Gating strategy	FCS-A/SSC-A followed by FSC-H/FSC-A polygonal gates were set to select single cells. For the Annexin V and CellROX channel, the gates were set in the minimum between the negative and the positive population using the positive control samples (TBHP). For the mGold channel the gate was set so that no mGold positive cells were present in the negative control (untreated).

☒ Tick this box to confirm that a figure exemplifying the gating strategy is provided in the Supplementary Information.